*Microscopy and Microanalysis*, 2025, **31**, ozae114
https://doi.org/10.1093/mam/ozae114
Advance access publication 26 November 2024
**Original Article**

Microscopy AND Microanalysis

# Spectral Pyrometry for Practical Temperature Measurement in the TEM

**D. Keith Coffman[1,*], Khalid Hattar[2], Jian Luo[3], and Shen Dillon[4]**

[1]*Department of Materials Science & Engineering, University of Illinois Urbana-Champaign, Champaign, IL 61801, USA*
[2]*Department of Nuclear Engineering, University of Tennessee Knoxville, Knoxville, TN 37996, USA*
[3]*Department of Materials Science & Engineering, University of California San Diego, Sand Diego, CA 92093, USA*
[4]*Department of Materials Science & Engineering, University of California Irvine, Irvine, CA 92697, USA*

***Corresponding author:** D. Keith Coffman, E-mail: devonc2@illinois.edu

## Abstract

Recent work in ultra-high temperature *in situ* electron microscopy has presented the need for accurate, contact-free temperature determination at the microscale. Optical measurement based on thermal radiation (pyrometry) is an attractive solution but can be difficult to perform correctly due to effects, such as emissivity and optical transmission, that must be accounted for. Here, we present a practical guide to calibrating and using a spectral pyrometry system, including example code, using a Czerny-Turner spectrometer attached to a transmission electron microscope. Calibration can be accomplished using a thermocouple or commercial heated sample holder, after which arbitrary samples can be reliably measured for temperatures above ~600°C. An accuracy of 2% can be expected with the possibility of sub-second temporal resolution and sub-Kelvin temperature resolution. We then demonstrate this capability in conjunction with traditional microscopic techniques, such as diffraction-based strain measurement for thermal expansion coefficient, or live-video sintering evolution.

**Key words:** spectral pyrometry, high temperature, laser heated, *in situ* TEM

## Introduction

Recent work in laser-heated *in situ* TEM studies has demonstrated the need for ultra-high temperature measurement within the microscope. Ultra-high temperature materials have been reported to withstand $T > 1,700$°C (Wyatt et al., 2023) and do not begin undergoing significant diffusional transport below 1,200°C. These temperatures are beyond the capability of commercially available TEM holders. Observing the evolution of metal and ceramic systems at high temperatures can reveal thermo-kinetic material properties such as diffusivity and surface energy (Moore et al., 1997; Grosso et al., 2020; Vikrant et al., 2020; Ding et al., 2021), as well as a mechanistic understanding of the steps that drive the sintering processes (Coffman et al., 2022*a*; Hussein et al., 2022; Dillon et al., 2023; Smith et al., 2023). Quantitative thermo-kinetic analysis of such data requires accurate measurements.

Typical contact-based approaches encounter significant challenges at ultrahigh temperatures, including the need for chemical compatibility with the sample, thermal stability within the vacuum, and distance from the measurement to the region of interest. Inter-diffusion of atoms between the sample and the probe can adversely affect both the accuracy of the probe and the properties of the sample under observation. Thermal transport between the sample and probe can lead to a difference between measurement and local sample value, as well as disturbing the temperature distribution. Methods previously used to quantify local temperature in the TEM include the use of electrical resistivity (Jawaharram et al., 2020), diffractive thermal expansion (Winterstein et al., 2015), and (Grosso et al., 2020), electron energy-loss spectroscopy (EELS) (Mecklenburg et al., 2015), a phase transition with an assumption of linear laser power output (Bonneaux & Guymont, 1999) and (Coffman et al., 2022*b*), and thermal diffuse scattering (TDS) behavior (He & Hull, 2012). These approaches are highly material-specific, and have limitations such as individual calibration of thermal resistance devices on the sample, error in lattice parameter strain measurements, the need for a particular plasmon resonance, uncertainty in laser output behavior, and thickness sensitivity, respectively. Nevertheless, such approaches have allowed for preliminary results in ultrahigh temperature materials to be published using novel TEM characterization techniques such as those in Moore et al. (1997), Ding et al. (2021), Vikrant et al. (2020), Grosso et al. (2020), Smith et al. (2023), Coffman et al. (2022*a*), Hussein et al. (2022), and Dillon et al. (2023). At first glance, pyrometry appears to be an attractive temperature measurement solution: it is contactless and thus need not be tailored to match the sample. However, pyrometry also comes with a set of challenges which turn a seemingly simple concept into a nuanced process.

Pyrometry is based on the measurement of electromagnetic radiation emitted by thermal vibration of charges within the sample. The detection of this radiation is modified by several physical processes, including the sample surface itself ("emissivity"), the optical components collecting the light, the dispersive element of the spectrometer, the quantum efficiency of the CCD pixel generating charge from photons, and the readout process converting accumulated charge into a digital count. The process of inferring temperature from spectrometer readout therefore becomes an exercise in modeling the

**Received:** May 16, 2024. **Revised:** October 7, 2024. **Accepted:** October 29, 2024

detection system itself, with the true sample temperature being just one of several parameters that contribute to the observed output.

There is a healthy body of literature dealing with the issue of calibrating and applying spectral pyrometry to samples with varying field of view and emissivity (Araújo, 2017). However, the TEM environment does pose some unique considerations compared to typical commercial or research settings. In the TEM, the small sample size means there is little light available to capture, particularly at low temperatures and with localized laser heating. Space between pole pieces is limited, meaning a calibrated light source cannot be placed easily in the chamber to account for optical dispersion. Lastly, high-throughput experimentation on a variety of samples makes the prospect of external validation of emissivity tedious.

This article and supporting document presents a model and calibration process which can be practically applied for *in situ* temperature measurement in the TEM, using only a thermocouple or otherwise temperature-sensitive holder for calibration, and an optical spectrometer for ongoing measurement. We address the issue of noise-limited emissivity fitting and provide some examples of the technique applied in conjunction with microscopy techniques that highlight its utility.

## Materials and Methods

Most of the details of implementation, including hardware, model parameters/equations, and code, are discussed in the supporting document. We have applied this technique on two different microscopes with differing hardware, illustrating the generality of the technique. In both systems, samples are locally heated using an 1,064 nm infrared laser and the thermal radiation is collected by a CZ spectrometer attached to the microscope via fiber optic. One system is located at the University of Illinois Urbana-Champaign (UIUC) Materials Research Lab, using a JEOL 2010 $LaB_6$ microscope equipped with an OceanOptics QE65000 spectrometer. The other is the $I^3$TEM system (Parrish et al., 2021) located in the Sandia National Laboratories' (SNL) Ion Beam Lab (IBL) equipped with an Andor Shamrock 303i spectrometer.

At a high level, the sample-spectrometer system is modeled, starting with the Planck equation and concluding with the analog-to-digital conversion circuit inside the spectrometer. Unknown system parameters are fit using a Nelder–Mead simplex optimization algorithm to minimize the difference between observed and modeled count spectrum, as illustrated in Figure 1. Among the fit parameters are the sample temperature and two sample emissivity parameters. Thus, the act of fitting the model produces a temperature measurement. The background signal (i.e. dark current and laser scatter) adds additional parameters to be fit. We see that the background is equal to the observed signal at low wavelengths because Planck's law asymptotically approaches zero, leaving only background sources to contribute to the count spectrum and making the parameter easy to fit. At high temperature, the background becomes negligible in comparison to the signal intensity.

The first time the model is run, there are many additional parameters that must be fit, namely a per-pixel "system efficiency" that accounts for the wavelength-dispersive elements between sample and readout. This calibration step must be done with a known temperature and spectral emissivity, and

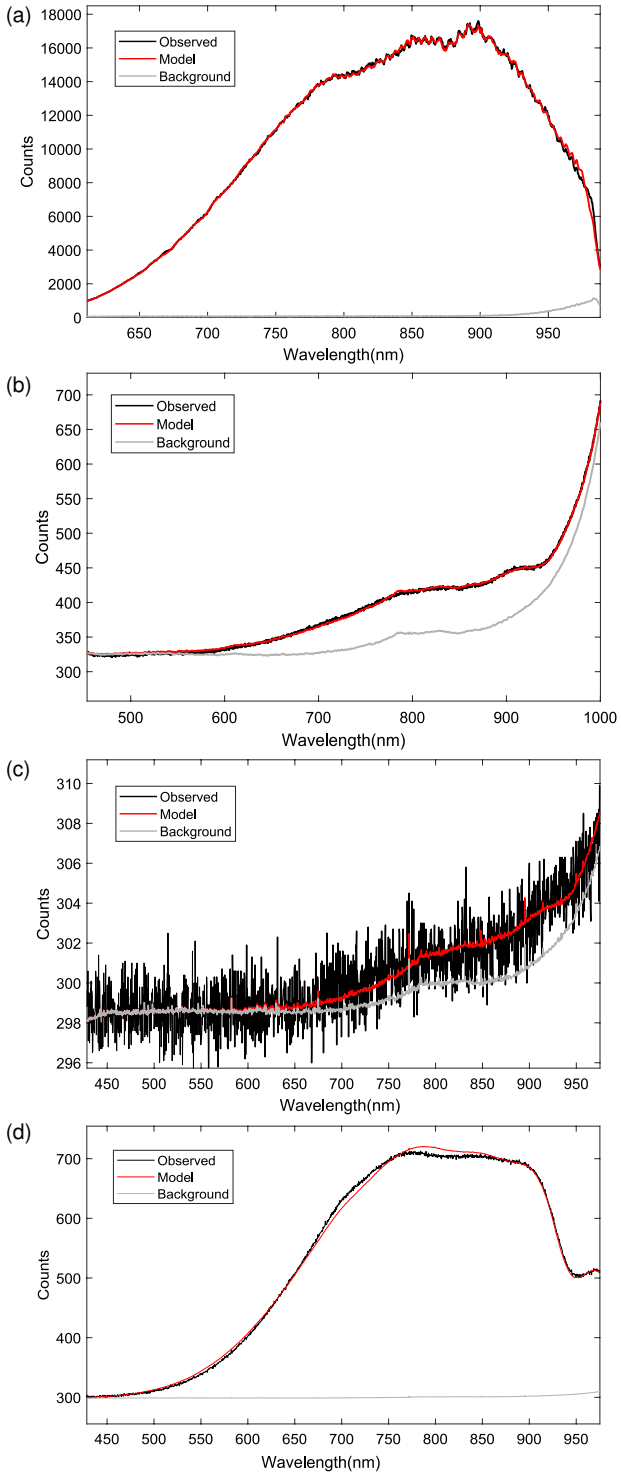


**Fig. 1.** Examples of spectra fit using the model described in the supporting document, and their estimated contributions from background sources (offset, dark current, and laser current). Shown are (**a**) Tungsten at 1,600°C, (**b**) $ZrO_2$ at 1,160°C, (**c**) $ZrO_2$ at 860°C, and (**d**) $ZrO_2$ at 1,375°C. In the low-temperature regime, reflections of the heating laser can dominate the signal. The spectrum in (**d**) demonstrates nonlinear emissivity, as the best-fit linear emissivity model still exhibits small ± deviations across the spectrum.

can be accomplished with a thermocouple or other temperature sensing method (theoretically, even a known phase transition will suffice). In the two systems used for this study,

one was accomplished with a commercial heating holder, while the other was accomplished with a laser-heated thermocouple wire.

### Emissivity Fitting

A key challenge in applying pyrometry is accounting for the wavelength-dependent emissivity of the sample surface. Spectral emissivity $\varepsilon(\lambda, T)$ is an intrinsic property of the sample and will vary between experiments and possibly within the experiment. Emissivity is sensitive to surface effects as well as the angle of observation. Tilting the sample during observation could change the apparent emissivity, as well as any effects of irradiation by the electron beam (e.g. oxidation/reduction) or heating (e.g. thermal etching).

In principle, the emissivity $\varepsilon_i$ at each pixel wavelength $\lambda_i$ adds a new unknown parameter to the problem that must be solved for in the model. In practice, the number of parameters that can be fit is limited by the complexity of the underlying blackbody function on the range of wavelengths measured by the spectrometer. Other works on the spectral pyrometry problem have shown that using more than two parameters to describe spectral emissivity generally results in no improvement in temperature estimation and can even make it worse (Araújo, 2017). Intuitively, if the Planck function $B(\lambda, T)$ on the range $[\lambda_0, \lambda_n]$ can be adequately described by a polynomial of degree $N$, we should expect to be able to fit temperature and an emissivity polynomial of degree $N-1$. In the UIUC system, the spectrometer range is 611–988 nm and the blackbody function can be described well with a degree of 2 for temperatures in the range of 1,000 to 3,000°C, as shown in Figure 2. Here, we illustrate a simple "noise floor" of 0.5% to determine where higher order fitting no longer benefits. Any error in fitting below this threshold is indistinguishable from noise. This 0.5% floor, i.e. a signal-to-noise ratio (SNR) of 200, reflects nonideal collection conditions likely to occur in a real experiment. A 16-bit CCD under ideal collection conditions is theoretically capable of higher SNR, but in practice, the exposure time will not always be optimal. Note that, for lower temperatures in particular, the noise floor will rise with the shot noise of a dim source. Thus, a higher order polynomial may not be advantageous for low temperatures even if the Planck function becomes increasingly nonquadratic.

Put another way, for our system we expect a spectrum to yield about three useful parameters. Consequently, we used an emissivity model of degree 1 as shown in equation (1):

$$\varepsilon(\lambda, T) \cdot B(\lambda, T) = \varepsilon_0[1 + \varepsilon_1(\lambda - \lambda_0)] \cdot \frac{2c}{\lambda^4}\left(\exp\left[\frac{hc}{\lambda k T}\right] - 1\right)^{-1}, \quad (1)$$

where $\varepsilon_0$, $\varepsilon_1$, and $T$ are the unknown parameters, and $\lambda_0$ is the central wavelength of the spectrometer. Fortunately, a linear emissivity in the optical range is common in some relevant metals such as tungsten (Cagran et al., 2005). This linear emissivity model is used to estimate temperature, but any deviations from the best-fit model can be measured, so a full spectral emissivity curve can be derived once the temperature is fit. Qualitative examination of this curve may indicate if a highly nonlinear spectral emissivity is present, as illustrated in Figure 1d. Note that variations in $\eta_{\text{fov}}$ (discussed in the supporting document) and $\varepsilon_0$ are indistinguishable. If the experimenter is interested in the absolute value of $\varepsilon_0$, they must estimate the change in $\eta_{\text{fov}}$ between calibration and subsequent measurements. If the sample is measured at multiple distinct temperatures, a greater internal consistency might be achieved by assuming that $\varepsilon_1$ is either constant or linearly temperature dependent:

$$\varepsilon_1(T) = \varepsilon_1^0 + \varepsilon_1^1 T. \quad (2)$$

The fitting process is then applied to a set of spectra, each having their own $T$ and $\varepsilon_0 \cdot \eta_{\text{fov}}$ values, but sharing a common $\varepsilon_1$ parameter, which helps to underfit the system. The literature suggests that the emissivity-wavelength slope in tungsten may vary somewhat with temperature, Cagran et al. (2005) hence the motivation for splitting $\varepsilon_1$ into $\varepsilon_1^0$ and $\varepsilon_1^1$.

It should be noted that assumption of the spectral emissivity of the sample during calibration is unavoidable, and any inaccuracy in this curve will manifest as a distortion of the inferred system efficiency curve relative to its true shape. Linear distortion of the system efficiency curve can be counteracted by the $\varepsilon_1$ parameter, but doing so will misrepresent the sample's true spectral emissivity. Thus, the user will get a linear approximation of the spectral emissivity "for free" with their measurement, but the accuracy of this value is dependent on the calibration.

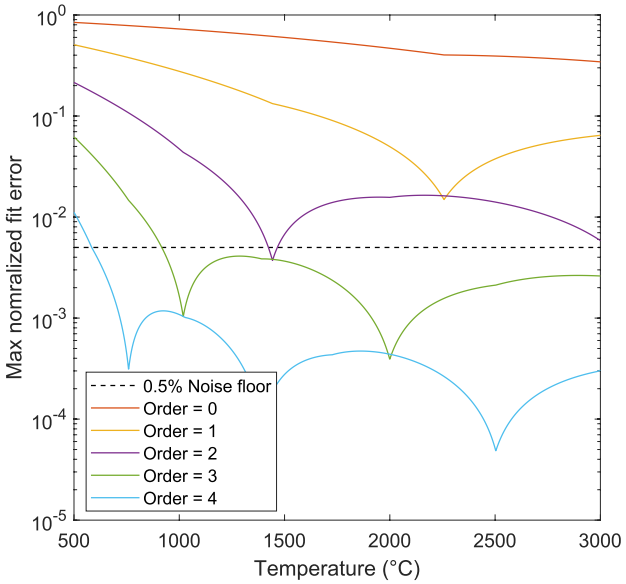


**Fig. 2.** Maximum error associated with fitting the Planck function in the range of 611 to 988 nm using polynomials of varying order. Maximum error, i.e. largest deviation from the true curve, is normalized by the peak signal at a given temperature. Dips occur when one order is particularly good at approximating the Planck function on this spectral domain, but they have no particular significance. As expected, a higher order provides a better fit, but above order 2 the error is smaller than the noise that might be expected in the data.

## Results and Discussion

The results of the calibration process for the two microscope systems studied are shown in Figure 3, including the spectra used, the resulting system efficiency curves, and the calculated temperatures. The filled marker indicates which spectrum was used as the reference in computing the system efficiency curve, while the open markers indicate temperatures fit from the resulting curve. The fitting process aimed to optimize agreement

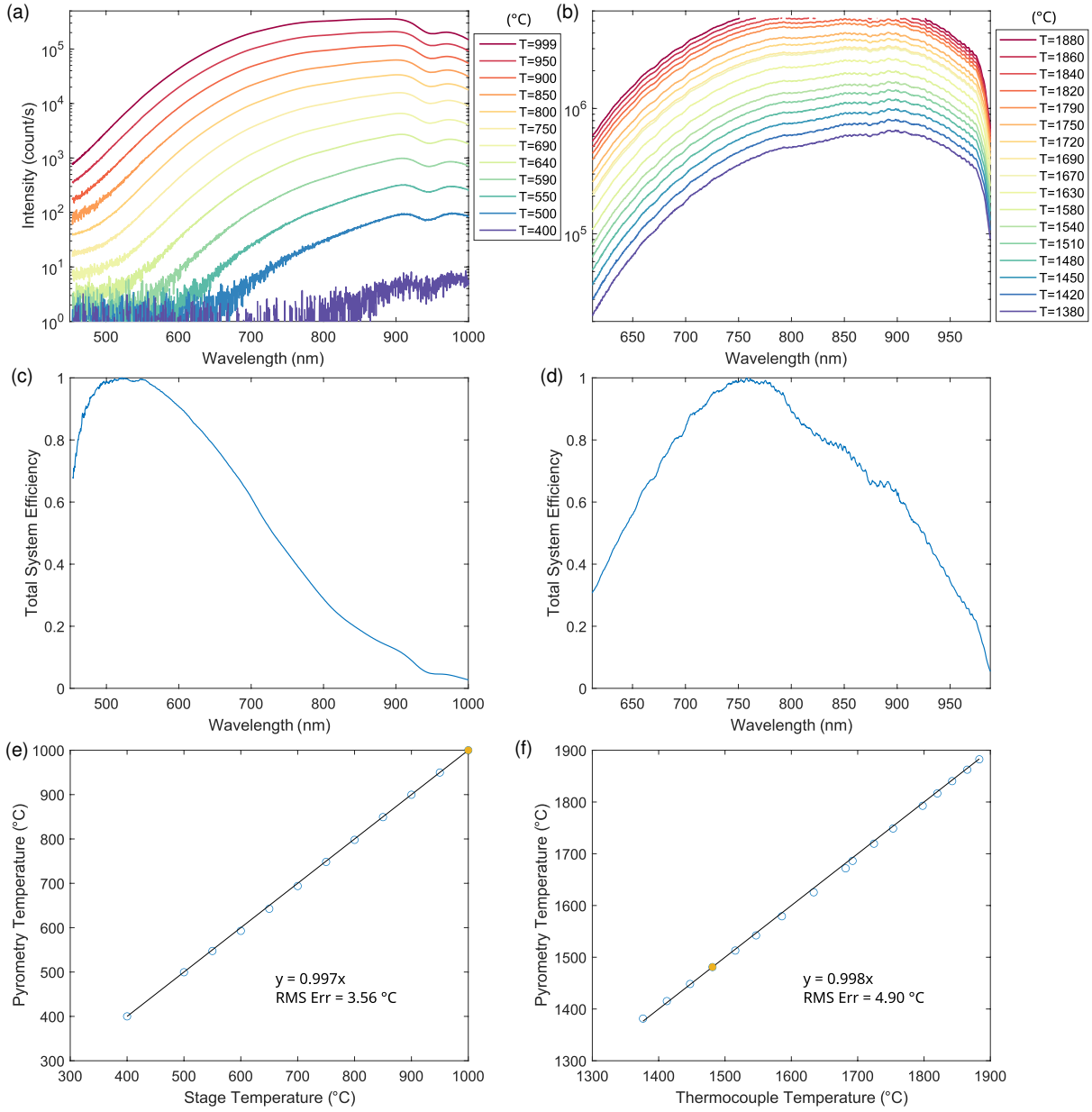


**Fig. 3.** Calibration of the Sandia (left) and UIUC (right) systems. (**a,b**) Captured spectra, (**c,d**) system efficiency curves, (**e,f**) comparison of temperatures as measured by thermocouple and as calculated using pyrometry. The filled marker indicates which spectrum was used in computing system efficiency. The Sandia system was calibrated using a Gatan 652 heating holder (tantalum) while the UIUC systems was calibrated using a type C thermocouple (tungsten) from Evolution Sensors & Controls, LLC.

across the entire temperature range, thus inaccuracies in both the thermocouple emissivity and the thermocouple temperature reading will influence in the calibrated parameters.

We can see that the process is internally consistent, with one assumed temperature reproducing the other observed temperatures to within 0.8% and 0.6% of the thermocouple value, respectively. We can also see that the two optical systems have substantially different system efficiency curves, attributed mainly to their diffraction gratings in this case. This highlights the importance of the calibration step.

Based on a variety of samples tested on each system, we found that the light output tends to become insufficient for temperature measurement around 600°C as discussed below. This limitation includes the highly localized nature of laser heating (a few $\mu$m), and reasonable integration times for the spectrometer. As can be seen in Figure 3e, a conventional heating holder with a larger heated volume (not laser heated) can extend this range somewhat to 400°C using the same uncertainty metric. Higher optical efficiencies should also extend the measurable temperature range.

## Accuracy and Precision

The temporal resolution of the technique is limited at high temperature by the spectrometer capture rate, and at low temperature by signal-to-noise ratio. Typical CCD-based spectrometers can capture every few milliseconds. Figure 4 shows a 20 ms cycle capturing individual thermal relaxation

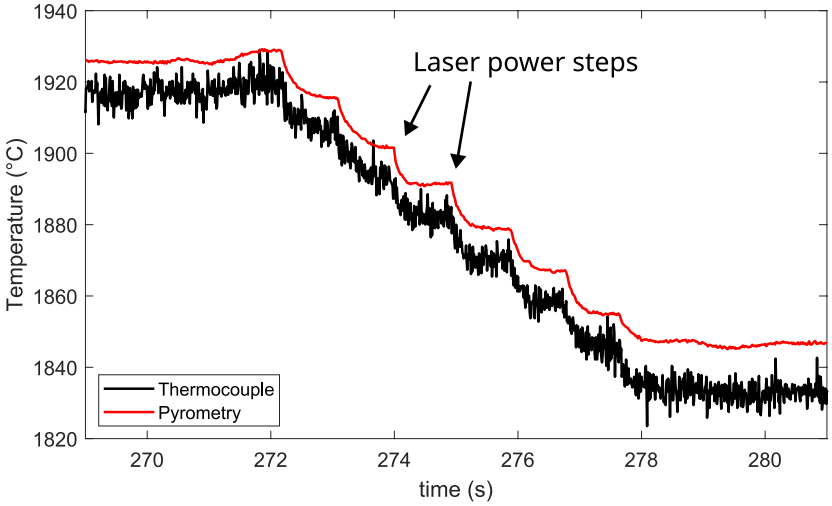


**Fig. 4.** Example of temporal resolution of the technique, with 20 ms intervals showing the response of a type C thermocouple to steps in laser power during imaging.

events associated with laser power steps. This figure also shows the relative stability of the measurement between captures, with an apparent temperature precision of <1.0°C.

Thermal precision is also temperature dependent, with high temperatures providing higher precision.

$$B(\lambda, T, \epsilon) \approx \epsilon \frac{2c}{\lambda^4}\left(\exp\left[\frac{hc}{\lambda k T}\right]\right)^{-1} \tag{3}$$

The primary source of inaccuracy in this technique arises from uncertainty in the spectral emissivity of the sample. Using the Wein approximation Wien (1897) to the Planck equation shown in equation (3), we can compare the expected spectral signal from two different pixels at different temperatures and emissivities. Dividing $B(\lambda_1, T_1, \epsilon_1)$ by $B(\lambda_2, T_2, \epsilon_2)$, where $T_1$ is the true temperature, $\epsilon_1$ is the emissivity at $\lambda_1$, and $T_2$ is the erroneous temperature arising from $\epsilon_2 = \epsilon_1 + \delta\epsilon$, we have

$$\frac{\Delta T}{T} = \left(1 - \frac{hc/k_b}{\lambda_1(1+\frac{\lambda_1}{\Delta\lambda})T\ln\left(1+\frac{\delta\epsilon}{\epsilon_1}\right)}\right)^{-1}. \tag{4}$$

In the context of the linear emissivity model in equation (1), $\delta\epsilon/\epsilon_1 = \delta\varepsilon_1\Delta\lambda/\varepsilon_0$ which gives

$$\frac{\Delta T}{T} = \left(1 - \frac{hc/k_b}{\lambda_1(1+\frac{\lambda_1}{\Delta\lambda})T\ln\left(1+\frac{\delta\varepsilon_1\Delta\lambda}{\varepsilon_0}\right)}\right)^{-1}. \tag{5}$$

For instance, a spectrometer with a range of 600 to 1000 nm at a temperature of 1,873°C and an emissivity error of $\delta\epsilon/\epsilon_1 = 0.1$ would have a temperature error of 1.9%. In the linear model, this corresponds to a slope error of $\delta\varepsilon_1 \approx 10^{-4}\,\mathrm{nm}^{-1}$. As shown in Figure 5, this is also approximately the uncertainty we might expect from the fitting process. In general, the lower temperature limit of this technique is determined by the acceptable level of uncertainty in the fit temperature. We found this value grows with lower temperature spectra, exceeding 10% below 600°C in our laser-heated samples, and below 400°C in our conventionally heated sample. There appears to be no upper limit to the technique, since the Planck function

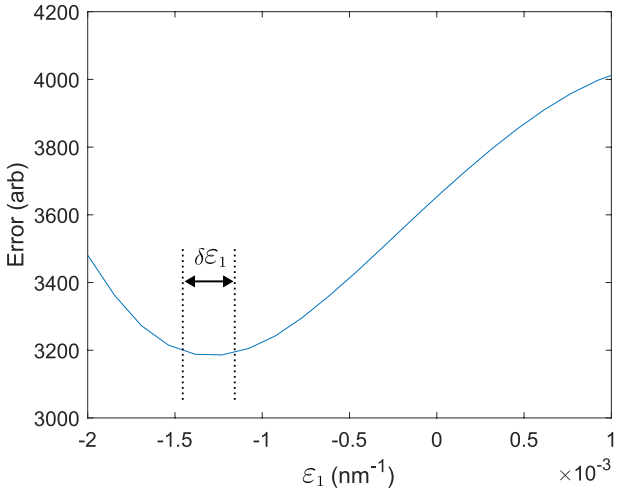


**Fig. 5.** Example of objective function versus fixed $\varepsilon_1$ for a $ZrO_2$ sample at 1,500°C. In the context of equation (5), this gives a sense of expected uncertainty of the temperature fit.

remains valid beyond the point at which samples will evaporate in the TEM.

For localized laser heating, the nonuniform temperature distribution within the sample might also affect the result. It is assumed in our work that the signal is dominated by the hottest points within the sample and that cooler regions have negligible impact on the spectrum. Work by Magunov (2010) shows that regions of $\Delta T > 10\%$ contribute essentially nothing to the calculated temperature, while closer temperatures exhibit varying degrees of spectral averaging. Still, the present approach can easily accommodate the addition of nonuniform distributions to the model if it becomes relevant to the application. One benefit of the code as-written is that its execution speed is feasible for live-capture.

The performance listed here is sufficient for a variety of previously difficult thermo-kinetic measurements, such as the activation enthalpies and volumes for transport and mechanical behaviors in ceramics. Such properties require the measurement of material response across a wide range (several hundred degrees) of high temperatures with accuracy. The

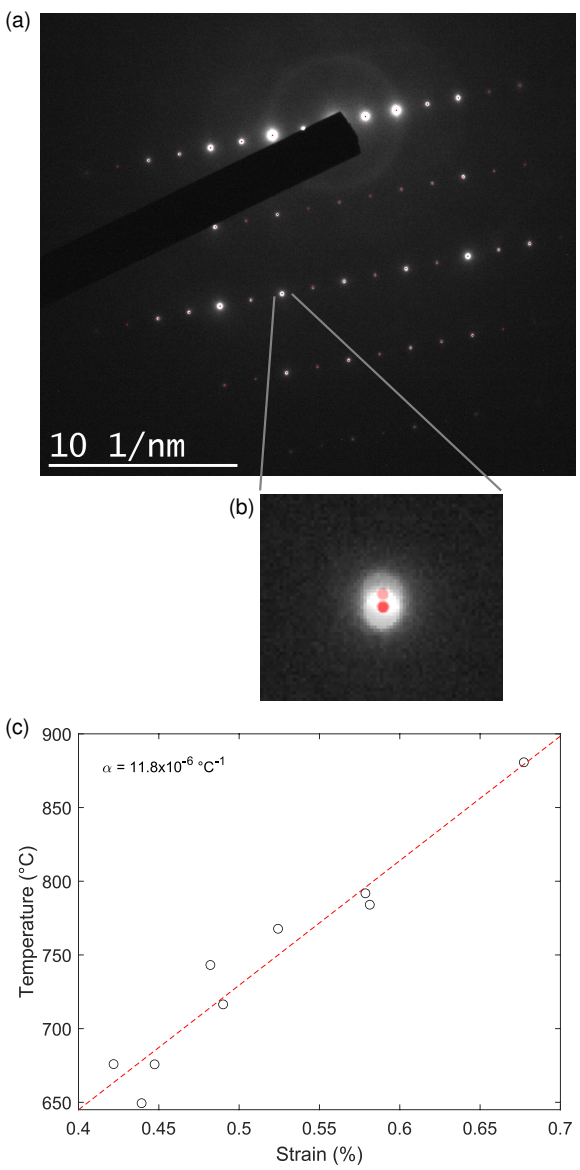


**Fig. 6.** Thermal expansion coefficient measured in a high entropy oxide using a combination of diffraction and spectral pyrometry. The diffraction pattern (**a**) is overlaid with red spots indicating the peaks used in strain measurement. (**b**) shows an example of the change in spot position between first and last measurement, on the order of 5 pixels or 0.05 $nm^{-1}$ for this spot. The lattice parameter for a given frame was fit using the best fit for the ensemble of spots with an estimated precision of 0.1%. The resulting thermal expansion is plotted in (**c**). The sample is a high entropy oxide of the following composition: $0.75[(Sm_{1/4}Eu_{1/4}Gd_{1/4}Yb_{1/4})_2(Ti_{1/2}Hf_{1/4}Zr_{1/4})_2O_7]$ $0.25[(Sc_{0.266}Dy_{0.248}Tm_{0.246}Yb_{0.240})_3NbO_7]$.

technique can be applied in tight spaces, such as the vacuum chamber of an SEM, TEM, or accelerator end station, making it a versatile tool for microscopy and microanalysis.

### *Thermal Expansion Measurement*

As a practical demonstration of the technique's complimentary utility to microscopy, we combined pyrometric temperature measurement with diffraction strain as a means of measuring coefficient of thermal expansion in a high entropy oxide (HEO) material, prepared by Luo and collaborators Wright et al. (2021). The strain $\epsilon$ can be calculated from a change in diffraction angle $g$ using equation (6)

$$\epsilon = \frac{g_0 - g}{g} \tag{6}$$

Diffraction patterns were obtained at various laser powers while spectra were recorded, and then the temperature and strain (relative to the unheated state) were calculated afterwards. The diffraction strain code used is included in the repository alongside the pyrometry code. Figure 6 shows a representative diffraction pattern from the sample and the thermal expansion observed. The thermal expansion for this material has not been previously measured, but the quantitative result of $11.8 \times 10^{-6}/^{\circ}C$ agrees with typical values for HEOs (Tang et al., 2022).

## Conclusions

The pyrometry technique presented here can be practically applied for *in situ* measurement of high temperatures in the TEM, and is especially useful in conjunction with localized laser heating of samples. The technique can be applied to samples of arbitrary composition, with minimal, unobstructive hardware, while providing high temporal and thermal resolution (<20 ms and <1°C). An accuracy of roughly 2% can be expected at high temperature, with a useful temperature range as low as 400°C and as high as the sample will withstand in vacuum. When used in conjunction with microscopy techniques, this can extend the capability of the TEM to measure thermal, thermodynamic, and kinetic properties of materials at high temperature.

## Availability of Data and Materials

Most of the code and data used in this work can be found at https://github.com/dcoffm/TEM-Pyrometry/

## Financial Support

This work is supported by funds from the National Science Foundation (DMR 1922867). The work was performed in part in the Materials Research Laboratory Central Research Facilities, University of Illinois, and in part at the Center for Integrated Nanotechnologies, an Office of Science User Facility operated for the U.S. Department of Energy (DOE) Office of Science by Los Alamos National Laboratory (Contract 89233218CNA000001) and Sandia National Laboratories (Contract DE-NA-0003525). J.L. acknowledges support from the National Science Foundation (Grant No. DMR-2026193) for fabricating the compositionally complex fluorite-based oxide (HEO) specimen used in this study.

## Conflict of Interest

No competing interest is declared.

## References

Araújo A (2017). Multi-spectral pyrometry—a review. *Meas Sci Technol* **28**(8), 082002. https://doi.org/10.1088/1361-6501/aa7b4b

Bonneaux J & Guymont M (1999). Study of the order–disorder transition series in AuCu by in-situ temperature electron microscopy. *Intermetallics (Barking)* 7(7), 797–805. https://doi.org/10.1016/S0966-9795(98)00128-9

Cagran C, Pottlacher G, Rink M & Bauer W (2005). Spectral emissivities and emissivity X-points of pure molybdenum and tungsten. *Int J Thermophys* **26**(4), 1001–1015. https://doi.org/10.1007/s10765-005-6680-1

Coffman DK, Ma Y, Barr C, Ouyang J-H, Hattar K & Dillon SJ (2022a). Evidence for interface-rate limited densification kinetics at $Al_2O3$-$GdAlO_3$ interfaces characterized by in situ ultrahigh temperature transmission electron microscopy. *J Eur Ceram Soc* **42**(13), 5904–5910. https://doi.org/10.1016/j.jeurceramsoc.2022.06.001

Coffman DK, Ma Y, Barr CM, Ouyang J-H, Hattar K & Dillon SJ (2022b). Interphase boundary, grain boundary, and surface diffusion in $Al_2O_3$-$GdAlO_3$ composites determined from bicrystal coble creep experiments. *J Eur Ceram Soc* **42**(9), 3976–3985. https://doi.org/10.1016/j.jeurceramsoc.2022.02.052

Dillon SJ, Lang E, Finkeldei SC, Ouyang J-H & Hattar K (2023). A nucleation rate limited model for grain boundary creep. *Acta Mater* **246**, 118718. https://doi.org/10.1016/j.actamat.2023.118718

Ding C, Chen W, Sabbaghianrad S, Xu J, Shan D, Guo B & Langdon TG (2021). In situ TEM observations of thickness effect on grain growth in pure titanium thin films. *Mater Charact* **173**, 110929. https://doi.org/10.1016/j.matchar.2021.110929

Grosso RL, Muccillo ENS, Muche DNF, Jawaharram GS, Barr CM, Monterrosa AM, Castro RHR, Hattar K & Dillon SJ (2020). In situ transmission electron microscopy for ultrahigh temperature mechanical testing of $ZrO_2$. *Nano Lett* **20**(2), 1041–1046. https://doi.org/10.1021/acs.nanolett.9b04205

Grosso RL, Vikrant KSN, Feng L, Muccillo ENS, Muche DNF, Jawaharram GS, Barr CM, Monterrosa AM, Castro RHR, García RE, Hattar K & Dillon SJ (2020). Ultrahigh temperature in situ transmission electron microscopy based bicrystal coble creep in Zirconia II: Interfacial thermodynamics and transport mechanisms. *Acta Mater* **200**, 1008–1021. https://doi.org/10.1016/j.actamat.2020.08.070

He L & Hull R (2012). Quantification of electron–phonon scattering for determination of temperature variations at high spatial resolution in the transmission electron microscope. *Nanotechnology* **23**(20), 205705. https://doi.org/10.1088/0957-4484/23/20/205705

Hussein O, Coffman DK, Hattar K, Lang E, Dillon SJ & Abdeljawad F (2022). Plateau–Rayleigh instability with a grain boundary twist. *Appl Phys Lett* **121**(14), 141601. https://doi.org/10.1063/5.0103658

Jawaharram GS, Barr CM, Monterrosa AM, Hattar K, Averback RS & Dillon SJ (2020). Irradiation induced creep in nanocrystalline high entropy alloys. *Acta Mater* **182**, 68–76. https://doi.org/10.1016/j.actamat.2019.10.022

Magunov AN (2010). Spectral pyrometry of objects with a nonuniform temperature. *Tech Phys* **55**(7), 991–995. https://doi.org/10.1134/S1063784210070121

Mecklenburg M, Hubbard WA, White ER, Dhall R, Cronin SB, Aloni S & Regan BC (2015). Nanoscale temperature mapping in operating microelectronic devices. *Science* **347**(6222), 629–632. https://doi.org/10.1126/science.aaa2433

Moore KI, Chattopadhyay K, Cantor B & Hirsch PB (1997). In situ transmission electron microscope measurements of solid Al-solid Pb and solid Al-liquid Pb surface-energy anisotropy in rapidly solidified Al-5% Pb (by mass). *Proc R Soc Lond A Math Phys Sci* **414**(1847), 499–507. https://doi.org/10.1098/rspa.1987.0156

Parrish RJ, Bufford DC, Frazer DM, Taylor CA, Gutierrez-Kolar J, Buller DL, Boyce BL & Hattar K (2021). Exploring coupled extreme environments via in-situ transmission electron microscopy. *Micros Today* **29**(1), 28–34. https://doi.org/10.1017/S1551929520001595

Smith J, Gao W & Chi M (2023). In situ investigation of the mechanistic causes of sintering in platinum–aluminum oxide catalysts. *Microsc Microanal* **29**(Supplement_1), 1613. https://doi.org/10.1093/micmic/ozad067.828

Tang A, Li B, Sang W, Hongsong Z, Chen X, Zhang H & Ren B (2022). Thermophysical performances of high-entropy $(La_{0.2}Nd_{0.2}Yb_{0.2}Y_{0.2}Sm_{0.2})_2Ce_2O_7$ and $(La_{0.2}Nd_{0.2}Yb_{0.2}Y_{0.2}Lu_{0.2})_2Ce_2O_7$ oxides. *Ceram Int* **48**(4), 5574–5580. https://doi.org/10.1016/j.ceramint.2021.11.101

Vikrant KSN, Grosso RL, Feng L, Muccillo ENS, Muche DNF, Jawaharram GS, Barr CM, Monterrosa AM, Castro RHR, García RE, Hattar K & Dillon SJ (2020). Ultrahigh temperature in situ transmission electron microscopy based bicrystal coble creep in zirconia I: Nanowire growth and interfacial diffusivity. *Acta Mater* **199**, 530–541. https://doi.org/10.1016/j.actamat.2020.08.069

Wien W (1897). On the division of energy in the emission-spectrum of a black body. *Lond Edinb Dubl Philos Mag J Sci* **43**(262), 214–220. https://doi.org/10.1080/14786449708620983

Winterstein JP, Lin PA & Sharma R (2015). Temperature calibration for in situ environmental transmission electron microscopy experiments. *Microsc Microanal* **21**(6), 1622–1628. https://doi.org/10.1017/S1431927615015196

Wright AJ, Wang Q, Hu C, Yeh Y-T, Chen R & Luo J (2021). Single-phase duodenary high-entropy fluorite/pyrochlore oxides with an order-disorder transition. *Acta Mater* **211**, 116858. https://doi.org/10.1016/j.actamat.2021.116858

Wyatt BC, Nemani SK, Hilmas GE, Opila EJ & Anasori B (2023). Ultra-high temperature ceramics for extreme environments. *Nat Rev Mater* **9**(11), 773. https://doi.org/10.1038/s41578-023-00619-0